AMS Home   Journals Home   Journal Archive   Subscribe   For Authors   Help   Advanced Search   [Search] Go

Full Text View

Dynamics of a Buoyancy-Driven Coastal Jet: The Gaspé Current

Jinyu Sheng

Department of Oceanography, Dalhousie University, Halifax, Nova Scotia, Canada

ABSTRACT

A primitive equation ocean model is applied to the process study of the Gaspé Current and cyclonic circulation over the northwestern Gulf of St. Lawrence (NWG). The model is driven by river discharge and barotropic boundary flows. Two types of model domains are used: an idealized basin with a flat bottom and piecewise coastline, and a realistic basin with model-resolved NWG bathymetry. The model domains are initially filled with horizontally uniform but vertically stratified waters. The river discharge is expressed in terms of lower salinity and a weak barotropic inflow in the upper waters at the estuary head.

The early developments of the estuarine plume and coastal current system driven by the river discharge are qualitatively similar in both basins. After a short-period adjustment, a buoyant plume is developed near the estuary mouth, with a surface-intensified coastal current advecting the estuarine water seaward in the direction of Kelvin wave propagation. The coastal current initially follows the coastline closely but later becomes unstable with backward-breaking waves developed along the outer edge of the current. The kinetic energy analysis reveals that the plume–current system is baroclinically unstable with the transient motions resulting primarily from the mean available potential energy.

With the river discharge at the head as the only driving force, the offshore front of the estuarine plume expands continuously seaward, leading to a large-scale anticyclonic circulation over the NWG. The addition of a barotropic westward jet along the Quebec shore, however, is able to restrain the seaward expansion of the offshore front of the plume, and therefore form a large-scale cyclonic motion over this region.

Options:
- Create Reference
- Email this Article
- Add to MyArchive
- Search AMS Glossary

Search CrossRef for:
- Articles Citing This Article

Search Google Scholar for:
- Jinyu Sheng

1. Introduction

The Gaspé Current is the most striking feature of near surface circulation in the Gulf of St. Lawrence. It also advects a large amount of freshwater downstream, affecting water properties and circulation over the Scotian Shelf and Gulf of Maine (Dickie and Trites 1983). The Gaspé Current is a buoyancy-driven coastal jet originating in the St. Lawrence Estuary. It is generally accepted that freshwater runoff from the St. Lawrence River drives a buoyant estuarine plume, with two distinct coastal currents flowing seaward separately along the north and south shores of the estuary (Fig. 1 ⬤▬). Combined with the cyclonic circulation of the northwestern Gulf of St. Lawrence (henceforth, NWG), the northshore current veers anticyclonically at the estuary mouth. This current flows southward and joins the current at the south shore, forming the root of the Gaspé Current (El-Sabh 1976). The Gaspé Current was found to reach its highest intensity of about 1 m s^{-1} around the Gaspé Peninsula, with a typical width of about 10–20 km in the top 50 m of the water column (Tang and Bennett 1981). It apparently leaves the coast at the eastern tip of the Gaspé Peninsula and carries buoyant estuarine waters onto the Magdalen Shallows (Fig. 1 ⬤▬).

The strength and position of the Gaspé Current vary significantly with time and space. From satellite infrared images, Tang (1980b) was the first to identify the occurrence of instabilities in the Gaspé Current under the summer high-runoff conditions. Mertz and El-Sabh (1989) later demonstrated that the unstable wave features also occurred in the autumn low-runoff conditions. The instability mechanisms responsible for the unstable wave development in the Gaspé Current, however, are less well understood. Tang (1980b) suggested that the wave motion of the current is triggered by barotropic instability, while Mertz et al. (1988) argued that both baroclinic and barotropic instabilities are operative in the region.

Estuarine plumes and buoyancy-driven coastal currents are common circulation features to many coastal regions in the world. Considerable analytical and laboratory studies have therefore been made in the past to gain better understanding of their main dynamics [see Hill (1998) for a comprehensive review]. Typically, an estuarine plume occurs at the estuary mouth when light estuarine waters spread over more saline coastal waters. For a wide estuary such as the St. Lawrence Estuary where the Coriolis effect is important, the buoyant estuarine plume turns anticyclonically and forms a surface-intensified coastal current that flows along the right-bounded coastline in the Northern Hemisphere.

One of the important features in the buoyant estuarine plume and associated coastal current system (henceforth, the plume–current system) is the development of eddies and instabilities. In the laboratory experiments of light density fluid flowing into a rotating channel initially filled with denser fluid, Stern (1980) and Griffiths and Linden (1981) found that wavelike disturbances appeared on the buoyancy-driven coastal current that was initially stable. The instabilities grew in amplitude, peeled off from the plume–current system, and formed eddies with a much slower translational velocity than the nose of the intrusion. Mavor and Huq (1996) observed very similar multiple instabilities along the outer edge of the current in their rotating turntable experiments.

Prognostic ocean models have been used increasingly in the study of plume–current systems (e.g., Wang 1985; Chao and Boicourt 1986; Chao 1988; Oey and Mellor 1993; Kourafalou et al. 1996). The main feature of a prognostic model is that temperature and salinity are updated as part of the solution procedure. Most of the previous numerical studies, however, concentrate mainly on the large-scale circulation features in a plume–current system. Oey and Mellor (1993) were the first to study the development of meanders and eddies in the coastal current using the Princeton Ocean Model. They found that the plume–current system undergoes two stages of the instability development: a barotropic stage characterized by short wavelength, and a baroclinic stage characterized by long wavelength. The main objectives of this paper are 1) to study the processes of the Gaspé Current and associated unstable waves driven by buoyancy forcing associated with freshwater discharge, and 2) to examine the combined effects of the river discharge and a barotropic westward jet along the Quebec shore on the formation of a large-scale cyclonic motion over the northwestern gulf of St. Lawrence (NWG). The eddy-resolving ocean model known as CANDIE (Sheng et al. 1998) is used in the study.

Note that the process study presented in this paper excludes the influence of wind and tides. Based on the occurrence of the minimum transport in the Gaspé Current during the period of the summer weakening of wind stress, Mertz et al. (1991) speculated that the cyclonic wind stress distribution over the NWG may be partially responsible for the formation of the cyclonic NWG circulation. Detailed numerical studies of the Gaspé Current and cyclonic circulation with the addition of wind stress and tidal mixing, however, remain to be done.

Section 2 summarizes the main features of observations in the summer months over the NWG. Section 3 describes the model configurations used in the numerical experiments. Section 4 presents the model results in an idealized basin with a flat bottom and a piecewise-straight coastline. Section 5 presents the model results in a realistic basin of the model-resolved NWG bathymetry. Section 6 is the summary and conclusions.

2. Oceanographic observations

The mean state of motion over the NWG is maintained primarily by the density gradients resulting from the St. Lawrence River discharge. The annual mean St. Lawrence River discharge is about 0.018 Sv (Sv $\equiv 10^6$ m^3 s^{-1}), comparable to the

Mississippi River. The St. Lawrence River discharge also exhibits significant seasonal variations. During the period from 1950 to 1984, for example, its monthly mean discharge is about 0.014 Sv from September to March of the next year, but increases to more than 0.03 Sv in May and June (Koutitonsky and Bugden 1991). It is suggested that the peak discharge from the St. Lawrence in later spring is most likely to trigger the development of meanders and instabilities in the Gaspé Current during the summer season (from July to September). In this paper, therefore, we only discuss the summer mean climatology of temperature and salinity and use them to initialize the model.

a. Summer mean hydrography

Figure 2 shows the near surface temperature and salinity in summer over the NWG (the area marked by the dashed lines in Fig. 1). They were gridded using the Barnes' Algorithm from the hydrographic observations made at depths less then 11 m. The near surface water in summer warms up progressively from the southwestern shallow area to the northern part of the NWG, with the coldest water around the estuary mouth and northern part of Jacques Cartier Strait (Fig. 2a). Along the Gaspé Peninsula, the near surface temperature in summer is relatively uniform.

By contrast, the near surface salinity in summer varies significantly around the estuary mouth and along the coastal region of the Gaspé Peninsula, with lower salinity closer to the shore. Over the northern part of the NWG, the near surface salinity in summer is relatively uniform. The combination of strong cross-shore variations in the near surface salinity and relatively weak alongshore variations in the near surface temperature along the Gaspé Peninsula indicates the predominance of the salinity distribution in driving the buoyancy-driven coastal current (i.e., Gaspé Current).

Figure 3a presents vertical profiles of summer mean temperature and salinity horizontally averaged over the NWG. The summer water column over the region can be described as a three-layer system: a warm and relatively fresh surface layer, a cold intermediate layer, and a warmer and saltier bottom layer. Figure 3b presents the vertical profile of density calculated from the temperature and salinity profiles. The density difference between the near surface and at 250 m is about $5\sigma_t$ (i.e., 5×10^3 kg m^{-3}). By assuming the horizontal scale of motion to be much larger than the vertical scale and ignoring the nonlinear terms, the baroclinic modes were calculated based on the vertical density profile using the method outlined by Kundu (1990, see chapter 13). Figure 3c shows the pressure eigenfunctions of the first three baroclinic modes. The baroclinic Rossby radii of deformation $r_i = c_i/f$ are about 10, 5.5, and 3.7 km respectively, for the first three baroclinic modes, where f is the Coriolis parameter.

b. Summer mean current-meter observations

Figure 4 shows summer mean current-meter observations with record lengths longer than 15 days in the upper ocean (10–40 m) and in the lower ocean (90–220 m), respectively. Tides were removed before calculating the mean (Gregory et al. 1989). Horizontal averaging was performed if means were available within 10 km of each other.

The summer mean upper-ocean current-meter observations (Fig. 4a) exhibit significant spatial variabilities, particularly over the estuary mouth. Nevertheless, they suggest a transverse flow with typical speed of about 10 cm s^{-1} near the estuary mouth and a strong coastal current known as the Gaspé Current with a maximum speed of about 50 cm s^{-1} along the Gaspé Peninsula. They also suggest a large-scale cyclonic motion over the NWG region.

In the lower ocean the time-mean current-meter observations (Fig. 4b) are much weaker than those in the upper ocean, particularly near the estuary mouth and along the Gaspé Peninsula, indicating the surface-intensified characters of the Gaspé Current.

c. Satellite images of sea surface temperature

Satellite images have been successfully used in the past to identify the Gaspé Current and associated unstable wave development (Tang 1980b; Mertz et al. 1988; Mertz and El-Sabh 1989). Figure 5 presents the drawings of backward-breaking waves in the Gaspé Current in August 1978 based on the satellite images shown by Tang (1980b). Similar drawings were also made by Mertz et al. (1988) and Reszka and Swaters (1999). Backward-breaking waves are the baroclinic waves on the density fronts that have a tendency to "break" in the upstream direction and to yield an often sharp crested steamer pointing upstream (Griffiths and Linden 1981). Figure 5 shows three well developed backward-breaking waves on 6 August 1978. They grew into large sizes and tended to break upstream about one day later. The typical wavelength of these waves are about 60 km.

3. Model description

Numerical experiments were made using CANDIE, a three-dimensional primitive equation z-level ocean model. Its main

features, including the subgrid-scale mixing parameterizations, are summarized in the appendix. Sheng et al. (1998) recently applied this model to a standard test problem of wind-driven circulation over an idealized coastal canyon. They found that CANDIE performs well in comparison with other ocean models. In the present application, CANDIE was forced by freshwater fluxes and barotropic boundary flows. The surface wind and surface heat–salinity fluxes were set to zero. Note that, unless otherwise stated, the vertical eddy viscosity and diffusivity coefficients were set to 1 cm^2 s^{-1}, and horizontal eddy viscosity and diffusivity coefficients were determined using the Smagorinsky scheme.

Two types of model domains were used. The first is an idealized basin with a piecewise-straight coastline and a flat bottom of 200 m (Fig. 6a). It resembles the geometry of the NWG marked by dashed lines in Fig. 1 . The coastline of this idealized basin consists of two right convex corners, one at the northeast exit of the estuary (upstream corner), and the other downstream (downstream corner). The second domain is a realistic basin with the model-resolved NWG bathymetry (Fig. 6b). The dimension of the estuary in both basins is about 40 km wide and 70 km long. The estuary Kelvin number $K = W/r_1$ is about 4, where W is the estuary width and r_1 is the first baroclinic Rossby radius of deformation, indicating the importance of the Coriolis effect over the estuary region.

The model grid sizes in both basins are about 3.1 and 2.3 km in the east and north, respectively. This horizontal resolution was found to be sufficient to resolve baroclinic currents with typical length scales of the first baroclinic Rossby radius, about 10 km as discussed above. The vertical grid spacing is uniformly 10 m in the idealized basin. In the realistic basin the vertical grid spacing is uniformly 10 m from surface to 140 m. Below 140 m the vertical cell boundaries are at depths of 152, 168, 189, 218, 257, 310, and 370 m, respectively.

CANDIE was initialized with the summer mean vertical profiles of temperature and salinity shown in Fig. 3a and zero velocity everywhere except the estuary head (Fig. 6). To simulate the summer mean St. Lawrence river discharge in the model, the water mass in the top 30 m of the water column at the estuary head was maintained to be 10 ppt fresher than the summer mean salinity. A weak barotropic eastward inflow of 1.1 cm s^{-1} was also specified in the top 30 m at the head to represent the summer mean river discharge of 0.014 Sv. The temperature stratification at the head was set to be the same as the summer mean. Note that the buoyancy forcing associated with lower salinity at the head plays a predominant role in driving the circulation over the NWG region. The barotropic eastward inflow specified at the head is of secondary importance (see discussion in section 4e).

At the model lateral closed boundaries, the normal flow, tangential stress of the currents and horizontal fluxes of temperature and salinity were set to zero (free-slip conditions). Along the eastern and southern open boundaries, an explicit Orlanski radiation condition (Orlanski 1976) was applied for normal flow, temperature and salinity fields at each z-level.

4. Idealized basin experiments

The driving force for the numerical results presented in this section is the river discharge specified as lower salinity and a weak barotropic eastward flow in the top 30 m at the estuary head. Note that most of the previous numerical studies on the plume–current system were also made in an idealized basin (Chao and Boicourt 1986; Chao 1988; Oey and Mellor 1993). The present idealized basin experiments differ from others, mainly in three ways. The present model geometry consists of a wide estuary and a piecewise-straight coastline that introduce additional dynamical characteristics of the plume–current system. The water depth of the present basin is 200 m, much deeper than those used by others. Furthermore, the model basin, except the estuary head region, was initially filled with horizontally uniform but vertically stratified waters.

a. Estuarine surface outflow and onset of the coastal current

The model-produced onset of buoyancy-driven circulation driven by the river discharge in this idealized basin is very similar to that in the "dam-break" laboratory experiment (Stern et al. 1982) and the numerical simulation of buoyancy-driven circulation in a channel (Wang 1985; Chao and Boicourt 1986). Only a brief summary is given as follows.

Shortly after the model initialization, a zonal pressure gradient is created due to the density difference around the estuary head. This zonal pressure gradient drives an eastward surface current that advects the buoyant estuarine water downstream. Due to the Coriolis effect, this near-surface current veers southward and forms a strong southward jetlike stream along the offshore front of the estuarine plume (Fig. 7). At the north and south shores of the estuary, the Coriolis term in the zonal momentum equation vanishes, leading to a balance between the zonal pressure gradient and the inertial terms in the momentum equation over these two areas. Consequently, the buoyant estuarine waters along both shores spreads gradually eastward. The southward jetlike stream along the offshore front of the plume turns cyclonically over the turning area at the south shore, forming a narrow coastal current that flows eastward along the coast in the direction of Kelvin wave propagation.

b. Plume–current system and unstable wave development

The coastal current driven by the river discharge in the idealized basin follows the coastline closely during the first few days of simulation. Instabilities, however, start to develop after 10 days. Figure 8 presents the time sequence of near-surface salinity and flow fields produced by the fully nonlinear CANDIE model.

The plume–current system has become well developed by day 10, with a pool of accumulated estuarine waters and an intense semicircular anticyclonic eddy generated at the downstream corner (Fig. 8a). The near surface current inside this anticyclonic eddy abruptly turns cyclonically at the coast to south of the corner, acting as a transition zone connecting the eddy and the coastal current farther south (Chao and Boicourt 1986). Note that the appearance of a small-scale wavelike pattern along the outer edge of the current at day 10 represents the early development of baroclinic instabilities to be discussed later.

By day 30, the offshore salinity front of the estuarine plume has expanded downstream significantly and the anticyclonic eddy at the downstream corner has grown into a very large size with its center moving to about 70 km eastward from the corner (Fig. 8b). At day 50, the anticyclonic eddy at the downstream corner nearly pinches off from the plume–current system, with a new small-scale anticyclonic eddy created (Fig. 8c). A particularly interesting feature in Fig. 8c is the development of three noticeable backward-breaking waves along the edge of the plume–current system: one about halfway between the upstream corner and offshore front of the plume, and two to the south of the downstream corner.

The eddy-shedding phenomenon at the downstream corner is highly consistent with the laboratory experiment made by Klinger (1994). He observed the formation of an anticyclonic eddy when the current, which flows with the coast to its right in the downstream direction on the Northern Hemisphere, encounters a sharp obtuse corner of the angle not greater than 135°. He also found that this eddy grows in size and propagates diagonally away from the corner. As it moves away from the corner, a new anticyclonic eddy is created.

Note that the interactions of the anticyclonic eddy with the coast shown in Fig. 8 are qualitatively comparable to the conceptual model used by Nof (1988) for studying the collision of an isolated eddy with a vertical wall. He showed analytically that when a quasi-geostrophic anticyclonic vortex interacts with a wall, it leaks buoyant fluid only from its right hand side looking offshore in the northern Hemisphere.

c. Effects of momentum advection

The nonlinear advective terms in the horizontal momentum equations (i.e., $\mathcal{L}u$ and $\mathcal{L}v$ in the appendix) are most likely to play an important role in the instability development of the plume-current system shown in Fig. 8 . Their importance is usually measured by the Rossby number ϵ defined as U/fL, where U and L are typical velocity and length scales, respectively. In this idealized basin U and L are about 50 cm s^{-1} and 10 km (Fig. 8), respectively. The Rossby number ϵ is about 0.5, indicating that the dynamics governing the plume–current system are indeed nonlinear.

To further demonstrate the effect of the momentum advection on the instability development, CANDIE was linearized by eliminating the advective terms $\mathcal{L}u$ and $\mathcal{L}v$ from the horizontal momentum equations. Note that the advective terms in the conservation equations of temperature and salinity (i.e., $\mathcal{L}T$ and $\mathcal{L}S$ in the appendix) were retained. For simplicity, the experiment using this linearized model is referred as the linear case, and that using the fully nonlinear model as the nonlinear case.

Figure 9 shows the evolution of near-surface salinity and velocity fields in the linear case. Without advection terms in the momentum equations, the estuarine waters move along the coast in the direction of Kelvin wave propagation, with salinity isopleths and the coastal current following the coastline closely, indicating the dominant role of the momentum advection in generating eddies and instabilities in the nonlinear plume–current system. Furthermore, the lack of accumulation of buoyant estuarine waters at the downstream corner in the linear case implies that the momentum advection is also responsible for the eddy-shedding phenomenon at the downstream corner in the nonlinear case shown in Fig. 8 .

d. Kinetic energy analysis

An important question raised by the results shown in Fig. 8 is what type of instabilities is responsible for the unstable wave development in the nonlinear plume–current system. Barotropic instabilities grow by extracting kinetic energy from the mean flow field. Baroclinic instabilities, on the other hand, grow by converting mean potential energy to eddy flow (Holton 1992). To identify the main process responsible for the instability shown in Fig. 8 , I followed Ivchenko et al. (1997) and calculated the kinetic energy budget for the time-mean and eddy flows, where the eddy velocity is defined as the deviations from the time-mean flow. The governing equation for the kinetic energy for the mean flow (MKE) can be written as

$$\frac{\partial}{\partial t} \quad \quad \quad \quad \quad (1)$$

(see the appendix), where the notation ‹ › denotes the volume average, C represents advection of MKE through model open boundaries; N is the nonlinear exchange between MKE and kinetic energy of eddies; B is the exchange between MKE and mean available potential energy; F_h, F_v, F_b represent the dissipation of MKE through horizontal mixing, vertical mixing, and bottom friction, respectively; and R represents the generation of MKE by the buoyancy forcing associated with the river discharge.

The governing equation for the time mean kinetic energy of the transient flow, or time mean eddy kinetic energy (EKE) can be written as

$$\frac{\partial \langle \text{EKE} \rangle}{\partial t} = C' - N + B' + F'_h + F'_v + F'_b, \quad (2)$$

where C' represents advection of EKE through model open boundaries; B' represents the buoyancy production by the eddy flow; and F'_h, F'_v, and F'_b represent the dissipation of EKE through horizontal mixing, vertical mixing, and bottom friction, respectively.

Figure 10 ⦵ presents the total domain budget of MKE and EKE. The calculation was based on the model results between day 5 and day 80. The main energy source of the time mean flow is the buoyancy forcing associated with the river discharge at the estuary head. The conversion of MKE to the available potential energy (B) is about 85% of the buoyancy forcing at the head, predominant among all mean kinetic energy sinks. The main frictional mean kinetic energy sinks are lateral and vertical frictions (F_h and F_v). Note that the nonlinear kinetic energy convection (N), energy dissipation due to bottom friction (F_b), and energy loss due to boundary flows (C) are all relatively small, in comparison with B.

The sources of the eddy kinetic energy in order of magnitude are the buoyancy production by the eddy flow (B'), the nonlinear kinetic energy conversion (N), and a contribution by boundary flows (C'). The ratios of N/B' and C'/B' are about 20% and 5% respectively, indicating the predominance of the eddy buoyancy transfer as the kinetic energy source of the eddy flow. Since the nonlinear kinetic energy conversion N is generally interpreted as barotropic instability, it can be argued that the barotropic instability plays a minor role in generating eddies and instabilities in the nonlinear plume–current system shown in Fig. 8 ⦵.

Although the eddy buoyancy production B' is much larger than the nonlinear kinetic energy conversion N, the value of B', however, cannot be simply interpreted as the signature of baroclinic instability since other processes may also generate a B' transfer (Treguier 1992). Following Ivchenko et al. (1997), the exchange between the mean and eddy available potential energy was estimated based on

$$A' = \left\langle \frac{g \left(\overline{u'\rho'} \frac{\partial \overline{\rho}}{\partial x} + \overline{v'\rho'} \frac{\partial \overline{\rho}}{\partial y} \right)}{\rho_o \frac{d\tilde{\rho}(z)}{dz}} \right\rangle, \quad (3)$$

where $\tilde{\rho}(z)$ is the depth-dependent potential density of a reference state and was set to be the horizontally averaged initial potential density in this study.

A positive A' means that the mean available potential energy is converted to eddy available potential energy through baroclinic instability. The value of A' for the nonlinear plume–current system shown in Fig. 8 ⦵ is positive and about 1.2×10^{-3} cm^2 s^{-3}, which is about 60 times larger than B'. Since both eddy kinetic energy and eddy available potential energy are created mainly from the mean available potential energy, it can be concluded that the baroclinic instability processes are largely responsible for the unstable wave development in the nonlinear plume–current system shown in Fig. 8 ⦵.

e. Sensitivity study

A series of numerical experiments were conducted to examine the sensitivity of the model results to the subgrid-scale

mixing parameterizations and specification of the river discharge at the estuary head.

Figures 11a and 11b ⊙= present the near surface salinity fields at day 10 using the vertical mixing coefficients of 0.1 and 10 cm^2 s^{-1}, respectively. Other model parameters are the same as in Fig. 8 ⊙=. Larger vertical mixing weakens both the downstream expansion of the estuarine plume and the strength of the coastal current, highly consistent with the previous numerical studies (Chao and Boicourt 1986; Kourafalou et al. 1996).

Model results are also sensitive to the salinity difference and thickness of the upper low salinity waters (h_f) specified at the estuary head. This is not surprising since the salinity difference and upper water thickness h_f at the head determine the total potential energy available for driving the plume–current system. Figures 11c and 11d ⊙= show the near surface salinity fields at day 10 with the thickness h_f set to 10 and 40 m, respectively. Other model parameters are the same as in Fig. 8 ⊙=. A comparison of Figs. 11c,d ⊙= with Fig. 8a ⊙= demonstrates that an increase of h_f leads to more significant seaward expansion of the estuarine plume and a stronger coastal current with faster intrusion speed of the nose.

To examine the sensitivity of the model results to the barotropic eastward inflow specified at the estuary head, two experiments were made with the barotropic inflow set to zero and 5.5 cm s^{-1}, corresponding to the volume transport of 0 and 0.07 Sv, respectively. The model results using these two different inflows are very similar (Figs. 11e,f ⊙=). This is highly consistent with the results of Wang and Kravitz (1980). They found that a fivefold increase of the river inflow speed strengthens the plume-induced circulation by only 20%.

The general features of the plume–current system and associated unstable wave development using the no-slip boundary conditions (not shown) are also qualitatively similar to those using the free-slip conditions shown in Fig. 8 ⊙=. The major difference using the noslip and free-slip conditions is the anticyclonic eddy at the downstream corner that stays touching with the wall for a much longer time in the case of no-slip boundary conditions.

Four additional numerical experiments were conducted to investigate the effect of geometric shapes of the downstream corner on the plume–current system and corresponding instability development. Figure 12 ⊙= presents near-surface salinity fields at day 30 in four flat-bottom basins with different shapes of downstream corners. In the basin without a downstream corner (Fig. 12a ⊙=) the plume–current system is well developed along the straight coastline, with two noticeable backward-breaking waves created along the outer edge of the system. In the basin with a sharp obtuse corner of the angle less than 90° (Fig. 12b ⊙=), the overall feature of the estuarine plume and backward-breaking waves is quite similar to that in the first basin shown in Fig. 12a ⊙=, except a pool of estuarine waters and anticyclonic eddy formed at the downstream corner, indicating the importance of the sharp corner in generating this large-scale anticyclonic eddy, consistent with the laboratory findings by Klinger (1994). Figures 12c and 12d ⊙= show the model results in the basins with two slightly different configurations of the downstream corner. The basin in Fig. 12c ⊙= has two obtuse downstream corners and the one in Fig. 12d ⊙= has a rounded downstream corner. The fact of similar unstable wave developments in these two basins indicates the secondary importance of the curvature of the downstream corner to the development of backward-breaking waves.

5. Realistic basin experiments

Two sets of numerical experiments were conducted in the realistic basin. The model in the first set of experiments was forced only by the river discharge at the estuary head. In the second set of experiments the model was forced by the river discharge and a barotropic westward flow along the southern shore of Quebec.

a. River discharge at estuary head

CANDIE was first applied to the realistic basin forced by the river discharge at the estuary head, with the model parameters the same as those used in the idealized basin experiment presented in Fig. 8 ⊙=. Figure 13 ⊙= shows the near surface salinity and flow fields at day 10, 30, and 50, respectively. The coastal current at day 10 flows closely along the irregular coastline in the direction of Kelvin wave propagation, with small-scale meanders starting to develop along the outer edge of the current (Fig. 13a ⊙=), highly consistent with the idealized basin experiment shown in Fig. 8a ⊙=.

The buoyant estuarine plume in the realistic basin has expanded seaward significantly by day 30, also qualitatively similar to the idealized basin results (Figs. 8b and 13b ⊙=). Beyond the offshore salinity front of the plume, however, significant differences occur in the two basins. The coastal current in the realistic basin at this time becomes more unstable, with large-scale backward-breaking waves created along the outer edge of the coastal current (Fig. 13b ⊙=). By contrast, the backward-breaking waves are relatively small in the idealized basin at this time (Fig. 8b ⊙=). The other difference is the pool of estuarine waters and associated anticyclonic eddy that appear at the downstream right corner in the idealized basin but not in the realistic basin. Instead, a large amount of estuarine waters in the realistic basin has been advected onto the shallow

water region of the Magdalen Shallows (Fig. 13b ⊙). Note that the typical wavelength of the backward-breaking waves shown in Figure 13 ⊙ is about 90 km, which is similar but slightly larger than the wavelength of 60 km estimated from the satellite images of sea surface temperature (Fig. 5 ⊙).

By day 50 the buoyant estuarine water in the realistic basin has spread over most of the NWG region, with an intense large-scale anticyclonic eddy appearing over the area between the estuary mouth and the western tip of Anticosti Island (Fig. 13c ⊙). A small-scale but well-developed anticyclonic eddy is created over the area between the eastern tip of the Gaspé Peninsula and the Anticosti Island (Fig. 13c ⊙). To the south of this eddy several less well-developed eddies have been created with a southward drift onto the Magdalen Shallow. In the idealized basin, by contrast, the pool of buoyant waters tends to separate from the plume–current system near the downstream corner at this time (Fig. 8c ⊙).

A question arising from the above discussion is how important the variable bottom is to the development of the plume–current system. This problem was addressed by applying the fully nonlinear CANDIE model to the basin with the realistic coastline but a flat bottom of 400 m. All other model parameters are the same as before. During the first 10 days of simulation, the near-surface salinity and currents in the flat bottom case (not shown) are very similar to those in the basin with variable bottom, indicating the secondary importance of the variable bottom to the early development of the plume–current system. The influence of the variable bottom, however, becomes more important after 30 days of simulation. In particular, the coastal current in the flat bottom case follows the irregular coastline much more closely than that in the variable bottom case.

Figure 14 ⊙ presents the total domain budget of MKE and EKE in the realistic basin shown in Fig. 13 ⊙. The calculation was based on the model results between day 5 and day 80. The main kinetic energy source of the mean flow in the realistic basin is the buoyancy forcing associated with the river discharge at the estuary head, same as in the idealized basin experiment. The main kinetic energy sink of the time mean flow is the conversion of MKE to the available potential energy (B), which is about 90% of the buoyancy forcing at the head. The main frictional energy sinks are lateral and vertical frictions (F_h and F_v). Note that vertical friction is more important than lateral friction in dissipating mean kinetic energy in the realistic basin, in contrast to the flat-bottom idealized basin experiment. Similarly, the nonlinear kinetic energy conversion (N), energy dissipation due to bottom friction (F_b), and energy loss due to boundary flows (C) are all relatively small, in comparison with the mean buoyancy production (B).

The sources of eddy kinetic energy include, in order of magnitude, the eddy buoyancy production (B'), the nonlinear kinetic energy conversion (N), and boundary flow contribution (C'), same as in the flat-bottom idealized basin experiment. The ratios of N/B' and C'/B' are about 15% and 5%, respectively, indicating the predominance of the buoyancy transfer as the energy source of the eddy flow. Hence, the barotropic instability also plays a minor role in generating eddies and instabilities in the realistic basin. On the other hand, the value of A' for the nonlinear plume–current system shown in Fig. 13 ⊙ is positive and about 7.7×10^{-4} cm^2 s^{-3}, which is about 30 times larger than B'. It can be concluded, therefore, that the main instability process in the realistic basin is also baroclinic.

b. River discharge and a barotropic jet along the Quebec shore

One of the main features of the model results driven by the river discharge is the continuous seaward expansion of the buoyant estuarine plume with time. As a result, a large-scale anticyclonic motion is eventually created over the NWG region. This anticyclonic motion produced by the model is, however, contrary to common knowledge of general circulation over this region. Previous hydrographic studies have consistently revealed the presence of a quasi-permanent geostrophic cyclonic motion in this region (Trites 1972; El-Sabh 1976; Tang 1980a, 1983). The time-mean current meter observations in the upper ocean shown in Fig. 4 ⊙ also suggest the existence of this circulation feature. Clearly, other dynamic processes in addition to the St. Lawrence River discharge are engaged in the formation of the cyclonic circulation over the NWG region.

In this section, the role of a barotropic westward jet along the Quebec shore is examined in the formation of the cyclonic NWG motion. This is motivated by the findings of Petrie et al. (1988), showing that the Labrador Current enters the Gulf of St. Lawrence through the Strait of Belle Isle with volume transport up to 0.3 Sv. These Labrador Current waters are thought to flow westward along the Quebec shore and are entrained into the cyclonic circulation in the northwest gulf region.

The fully nonlinear CANDIE model was then applied to the realistic basin forced by both the river discharge at the estuary head and a barotropic westward jet at the northeast corner of the eastern open boundary (henceforth referred to as the eastern boundary inflow). The speed and width of this eastern boundary inflow were set to about 15 cm s^{-1} and 30 km, respectively, corresponding to the volume transport of about 0.4 Sv. The salinity and temperature of this jet are the same as the initial fields. Other model parameters are the same as before. Figure 15 ⊙ shows the near-surface salinity and current fields at days 10, 30, and 50.

A comparison of the model results in Figs. 13 and 15 🔘 shows clearly that the westward coastal current along the Quebec shore effectively constrains the eastward expansion of the buoyant estuarine plume and strengthens the Gaspé Current along the Gaspé Peninsula. Furthermore, the combination of the westward coastal current along the Quebec shore and the eastward Gaspé Current along the Gaspé Peninsula forms a large-scale cyclonic circulation over the NWG region (Figs. 15b,c 🔘). After passing the eastern tip of the Gaspé Peninsula, the Gaspé Current separates from the coast, creating an offshore jet that flows onto the Magdalen Shallows with large-scale meanders.

Figure 16 🔘 shows the time-mean currents at 15-m depth averaged from the model results between day 5 and day 80. The time-mean currents at this depth agree qualitatively well with the summer-mean current meter observations made in the upper ocean (Fig. 4a 🔘), suggesting the importance of the joint effect of the river discharge at the estuary head and the westward flowing coastal jet along the Quebec shore to the general circulation in the NWG region.

6. Summary and discussion

The Gaspé Current and cyclonic motion are the most distinctive circulation features over the northwestern Gulf of St. Lawrence. The Gaspé Current is the surface-intensified coastal jet driven primarily by the outflow from the St. Lawrence River. This current is dynamically unstable with growing meanders and instabilities.

A primitive equation model was applied to the process study of the coastal current and associated eddy and instability generation over the NWG region. Two model domains are used. The first is an idealized basin with a flat bottom and piecewise straight coastlines. The other is the realistic basin of the model-resolved NWG bathymetry. The model results in both basins have similar early developments of the plume–current system: a buoyant plume is created inside the estuary with a strong eastward near-surface outflow along the north shore of the estuary. This outflow turns anticyclonically and flows southward along the salinity front of the plume near the estuary mouth. It abruptly turns cyclonically at the south shore to form a surface intensified coastal current that advects the buoyant estuarine water downstream in the direction of Kelvin wave propagation. The numerical experiments in both basins also demonstrated that the coastal current initially follows the coastline closely but later becomes unstable with multiple backward breaking waves created along the outer edge of the plume–current system. Based on the kinetic energy analysis of time mean flow and eddies, it was found that the instability process responsible for the unstable wave development in the two basins is mainly baroclinic. The barotropic instability only plays a secondary role.

With the river discharge at the estuary head as the only external forcing, however, the buoyant estuarine plume expands successively with time, leading to a large anticyclonic circulation over the NWG region. This is opposite to the quasi-permanent cyclonic gyre observed over this area. The addition of a barotropic westward jet specified at the northeast corner of the model domain is efficient to constrain the seaward expansion of the estuarine plume and strengthen the Gaspé Current. The combined effect of the river discharge at the estuary head and the westward coastal current along the Quebec shore results in the formation of a statistically stable cyclonic circulation over the NWG region.

REFERENCES

Chao S. Y., 1988: River forced estuarine plume. *J. Phys. Oceanogr*, **18**, 72–88. Find this article online

Chao S. Y., and W. C. Boicourt, 1986: Onset of estuarine plumes. *J. Phys. Oceanogr*, **16**, 2137–2149. Find this article online

Dickie L. M., and R. W. Trites, 1983: The Gulf of St. Lawrence. *Estuaries and Enclosed Seas,* B. H. Ketchum, Ed., Elsevier Scientific, 403–425.

El-Sabh M. I., 1976: Surface circulation pattern in the Gulf of St. Lawrence. *J. Fish. Res. Board Can*, **33**, 124–138. Find this article online

Gregory D. N., O. C. Nadeau, and D. Lefaivre, 1989: Current statistics of the Gulf of St. Lawrence and Estuary. *Can. Tech. Rep. Hydrogr. Ocean Sci.*, **120,** 178 pp.

Griffiths R. W., and P. F. Linden, 1981: The stability of buoyancy-driven coastal currents. *Dyn. Atmos. Oceans*, **5**, 281–306. Find this article online

Hill A. E., 1998: Buoyancy effects in coastal and shelf seas. *The Sea,* Vol. 10, K. H. Brink and A. R. Robinson, Eds., John Wiley and Sons, 21–622.

Holton J. R., 1992: *An Introduction to Dynamic Meteorology*. Academic Press, 511 pp.

Ivchenko V. O., A. M. Treguier, and S. E. Best, 1997: A kinetic energy budget and internal instabilities in the fine resolution Antarctic model. *J. Phys. Oceanogr*, **27**, 5–22. Find this article online

Klinger B. A., 1994: Baroclinic eddy generation at a sharp corner in a rotating system. *J. Geophys. Res*, **99**, 12515–12531. Find this article online

Kourafalou V. H., L. Y. Oey, J. D. Wang, and T. N. Lee, 1996: The fate of river discharge on the continental shelf, 1. Modeling the river plume and the inner shelf coastal current. *J. Geophys. Res*, **101**, 3415–3434. Find this article online

Koutitonsky V. G., and G. L. Bugden, 1991: The physical oceanography of the Gulf of St. Lawrence: A review with emphasis on the synoptic variability of the motion. *Can. Spec. Publ. Fish, Aquat. Sci*, **113**, 57–90. Find this article online

Kundu P. K., 1990: *Fluid Mechanics*. Academic Press, 638 pp.

Mavor T., and P. Huq, 1996: Propagation velocities and instability development of a coastal current. *Buoyancy Efforts on Coastal and Estuarine Dynamics*, D. G. Aubrey and T. C. Friedrichs, Eds. Amer. Geophys. Union, 59–69.

Mertz G., and M. I. El-Sabh, 1989: An autumn instability event in the Gaspé Current. *J. Phys. Oceanogr*, **19**, 148–156. Find this article online

Mertz G., M. I. El-Sabh, and D. Proulx, 1988: Instability of a buoyancy-driven coastal jet: The Gaspé Current and its St. Lawrence precursor. *J. Geophys. Res*, **93**, 6885–6893. Find this article online

Mertz G., V. G. Koutitonsky, and Y. Gratton, 1991: On the seasonal cycle of the Gaspé Current. *Can. Spec. Publ. Fish Aquat. Sci*, **113**, 149–152.

Nof D., 1988: Eddy-wall interactions. *J. Mar. Res*, **46**, 527–555. Find this article online

Oey L. Y., and G. L. Mellor, 1993: Subtidal variability of estuarine outflow, plume, and coastal current: A model study. *J. Phys. Oceanogr*, **23**, 164–171. Find this article online

Orlanski I., 1976: A simple boundary condition for unbounded hyperbolic flows. *J. Comput. Phys*, **21**, 251–269. Find this article online

Petrie B., B. Toulany, and C. Garrett, 1988: The transport of water, heat and salt through the Strait of Belle Isle. *Atmos.–Ocean*, **26**, 234–251. Find this article online

Reszka M. K., and G. E. Swaters, 1999: Numerical investigation of baroclinic instability in the Gaspé Current using a frontal geostrophic model. *J. Geophys. Res*, **104**, 25685–25696. Find this article online

Sheng J., D. G. Wright, R. J. Greatbatch, and D. E. Dietrich, 1998:: CANDIE: A new version of the DieCAST ocean circulation model. *J. Atmos. Oceanic Technol*, **15**, 1414–1432. Find this article online

Smagorinsky J., 1963: General circulation experiments with the primitive equation. I. The basic experiment. *Mon. Wea. Rev*, **91**, 99–165. Find this article online

Stern M. E., 1980: Geostrophic fronts, bores, breaking and blocking waves. *J. Fluid Mech*, **99**, 687–704. Find this article online

Stern M. E., J. A. Whitehead, and B.-L. Hua, 1982: The intrusion of a density current along the coast of a rotating fluid. *J. Fluid Mech*, **123**, 237–265. Find this article online

Tang C. L., 1980a: Mixing and circulation in the northwestern Gulf of St. Lawrence: A study of a buoyancy-driven current system. *J. Geophys. Res*, **85**, 2787–2796. Find this article online

Tang C. L., 1980b: Observation of wavelike motion of the Gaspé Current. *J. Phys. Oceanogr*, **10**, 853–860. Find this article online

Tang C. L., 1983: Cross-front mixing and frontal upwelling in a controlled quasi-permanent density front in the Gulf of St. Lawrence. *J. Phys. Oceanogr*, **13**, 1468–1481. Find this article online

Tang C. L., and A. S. Bennett, 1981: Physical oceanographic observations in the northwestern Gulf of St. Lawrence. Bedford Institute of Oceanography Data Series BI-D-810-6, Dartmouth, NS Canada, 127 pp.

Treguier A. M., 1992: Kinetic energy analysis of an eddy resolving, primitive equation model of the North Atlantic. *J. Geophys. Res*, **97**, 681–701. Find this article online

Trites R. W., 1972: The Gulf of St. Lawrence from a pollution point of view. *Marine Pollution and Sea Life,* M. Ruivo, Ed., FAO, Fishing News Books, 59–62.

Wang D. P., 1985: Numerical study of gravity currents in a channel. *J. Phys. Oceanogr*, **15**, 299–305. Find this article online

Wang D. P., and D. W. Kravitz, 1980: A semi-implicit two-dimensional model of estuarine circulation. *J. Phys. Oceanogr*, **10**, 441–454. Find this article online

---

APPENDIX

7. CANDIE and Subgrid-Scale Mixing Parameterizations

The governing equations used in the circulation model are essentially the same as those considered by Sheng et al. (1998), with the exception that Cartesian coordinates are used here. Using the rigid-lid, Boussinesq and hydrostatic approximations, the three dimensional primitive equations for an incompressible, stratified fluid can be expressed as

$$\frac{\partial u}{\partial t} + \mathcal{L}u - fv = -\frac{1}{\rho_o}\frac{\partial p}{\partial x} + \mathcal{D}_m u + \frac{\partial}{\partial z}\left(K_m \frac{\partial u}{\partial z}\right) \quad \text{(A1)}$$

$$\frac{\partial v}{\partial t} + \mathcal{L}v + fu = -\frac{1}{\rho_o}\frac{\partial p}{\partial y} + \mathcal{D}_m v + \frac{\partial}{\partial z}\left(K_m \frac{\partial v}{\partial z}\right) \quad \text{(A2)}$$

$$\frac{\partial p}{\partial z} = -\rho g \quad \text{(A3)}$$

$$\frac{\partial u}{\partial x} + \frac{\partial v}{\partial y} + \frac{\partial w}{\partial z} = 0 \quad \text{(A4)}$$

$$\rho = \rho(T, S, p) \quad \text{(A5)}$$

$$\frac{\partial T}{\partial t} + \mathcal{L}T = \mathcal{D}_h T + \frac{\partial}{\partial z}\left(K_h \frac{\partial T}{\partial z}\right) \quad \text{(A6)}$$

$$\frac{\partial S}{\partial t} + \mathcal{L}S = \mathcal{D}_h S + \frac{\partial}{\partial z}\left(K_h \frac{\partial S}{\partial z}\right), \quad \text{(A7)}$$

where u, v, w are eastward, northward, and vertical components of the velocity, respectively; p is pressure; ρ is density; f is the Coriolis parameter; g is the gravitational acceleration; ρ_o is a reference density; K_m and K_h are the vertical eddy viscosity and diffusivity coefficients; $\mathcal{L}$ is an advection operator defined as

$$\mathcal{L}q = u\frac{\partial q}{\partial x} + v\frac{\partial q}{\partial y} + w\frac{\partial q}{\partial z}; \quad \text{(A8)}$$

and $\mathcal{D}_m$ and $\mathcal{D}_h$ are diffusion operators defined as

$$\mathcal{D}_{m,h}q = \frac{\partial}{\partial x}\left(A_{m,h}\frac{\partial q}{\partial x}\right) + \frac{\partial}{\partial y}\left(A_{m,h}\frac{\partial q}{\partial y}\right), \qquad (A9)$$

where A_m and A_h are the horizontal eddy viscosity and diffusivity coefficients.

In this paper the vertical mixing coefficients K_m and K_h were set to constants. The horizontal mixing coefficients $A_{m,h}$ were parameterized in terms of the horizontal grid length δ and the local deformation rate of the horizontal velocity field, following [Smagorinsky (1963)](#):

$$A_{m,h} = \max\left\{\alpha\delta^2\left[\left(\frac{\partial u}{\partial x} - \frac{\partial v}{\partial y}\right)^2 + \left(\frac{\partial v}{\partial x} + \frac{\partial u}{\partial y}\right)^2\right]^{1/2}, A_{\min}\right\}, \qquad (A10)$$

where $(\partial u/\partial x - \partial v/\partial y)$ and $(\partial v/\partial x + \partial u/\partial y)$ are the tension and shearing strain of horizontal flow, respectively, $\alpha = 0.28^2$ and $A_{\min} = 50 \text{ m}^2 \text{ s}^{-1}$.

In examining the kinetic energy balance of the model results, we decomposed the model results into their time-mean part (time-mean field) and a deviation from the mean (eddy field):

$$\mathbf{u} = \mathbf{U} + \mathbf{u}'; \qquad w = W + w'; \qquad p = P + p';$$

$$\rho = \bar{\rho} + \rho', \qquad (A11)$$

where $\mathbf{U}$, W, P, and $\bar{\rho}$ are the mean fields and $\mathbf{u}'$, w', p', and ρ' are eddy fields. Both $\mathbf{U}$ and $\mathbf{u}'$ are the velocity vectors of horizontal components.

The kinetic energy balances for the time-mean flow eddies can be obtained by multiplying the horizontal momentum equations [(A1)–(A2)] by the time-mean and eddy components of the velocity, respectively. Let ‹ › be the volume average defined as $\langle q \rangle = 1/V(\int_{(V)} q\, dV)$, the governing equation for MKE can be written as

$$\frac{\partial \langle \text{MKE} \rangle}{\partial t} = C + N + B + F_h + F_v + F_b$$

$$+ F_\tau + R \qquad (A12)$$

where

$$B = -\left\langle \frac{g}{\rho_o}\overline{\rho}W \right\rangle, \tag{A15}$$

where C represents the advection of mean kinetic energy by mean flow, pressure, and Reynolds stresses, respectively. Based on Gauss's theorem that the volume integral of a divergence term can be transformed into a surface integral, C can be interpreted as the advection of the MKE through model open boundaries. For a close basin, C is identical to zero. Here, N is the nonlinear exchanges between mean and eddy kinetic energy, and B is the exchange between mean kinetic and potential energy, respectively. Also, F_h, F_v, and F_b represent the dissipation (or generation) of mean kinetic energy through horizontal mixing, vertical mixing, and bottom friction processes, respectively; F_τ is the generation of MKE by wind forcing, and R is the generation of MKE by the buoyancy forcing associated with the river discharge.

The governing equation for the time mean kinetic energy of the eddy flow (EKE) can be written as

$$\frac{\partial \langle \text{EKE} \rangle}{\partial t} = C' - N + B' + F'_h + F'_v$$
$$+ F'_b + F'_\tau, \tag{A16}$$

where

$$C' = -\left\langle \nabla \cdot \left[k\mathbf{U} + \frac{\overline{p'\mathbf{u}'}}{\rho_o} + \frac{1}{2}\overline{(\mathbf{u}' \cdot \mathbf{u}')\mathbf{u}'} \right] \right.$$
$$\left. + \frac{\partial}{\partial z}\left[kW + \frac{\overline{p'w'}}{\rho_o} + \frac{1}{2}\overline{(\mathbf{u}' \cdot \mathbf{u}')w'} \right] \right\rangle \tag{A17}$$

$$B' = -\left\langle \frac{g}{\rho_o}\overline{\rho'w'} \right\rangle \tag{A18}$$

$$F'_h = \langle \overline{\mathbf{u}' \cdot \mathcal{D}_m\mathbf{u}} \rangle \tag{A19}$$

$$F'_v = \left\langle \overline{\mathbf{u}' \cdot \frac{\partial}{\partial z}\mu_m\frac{\partial \mathbf{u}}{\partial z}} \right\rangle, \tag{A20}$$

where C' represents advection of eddy kinetic energy through model open boundaries; B' represents the buoyancy production by the eddy flow; F'_h, F'_v, and F'_b represent the dissipation (or generation) of eddy kinetic energy through horizontal mixing, vertical mixing, and bottom friction, respectively; and F'_τ is the generation of EKE due to the wind forcing.

Figures
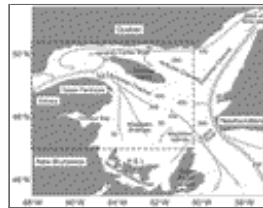
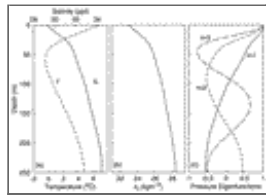Click on thumbnail for full-sized image.

FIG. 1. Main bathymetric features of the Gulf of St. Lawrence and schematic presentations (light gray arrows) of large-scale

circulation in the region. The area marked by the dashed lines is the model domain
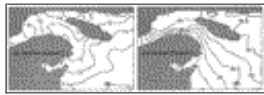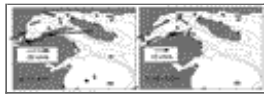

Click on thumbnail for full-sized image.

FIG. 2. Summer mean near-surface (0–11 m) fields of (a) temperature and (b) salinity gridded from hydrographic data using Barnes' algorithm
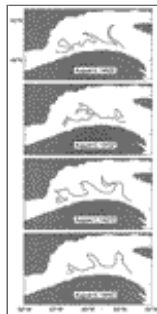

Click on thumbnail for full-sized image.

FIG. 3. Vertical profiles of (a) temperature and salinity spatially averaged from the gridded hydrographic data over the northwestern Gulf of St. Lawrence, (b) in situ density calculated from the vertical temperature and salinity profiles shown in (a), and (c) pressure eigenfunctions of the first three baroclinic modes calculated based on the vertical density profile shown in (b)

Click on thumbnail for full-sized image.

FIG. 4. Time mean current-meter observations in summer with record lengths longer than 15 days in the (a) upper ocean (10–40 m) and (b) lower ocean (90–220 m) over the northwestern Gulf of St. Lawrence

Click on thumbnail for full-sized image.

FIG. 5. The drawings of evolution of backward-breaking waves in the Gaspé Current in Aug 1978 based on the infrared satellite images of sea surface temperature shown by Tang (1980b). Only the outer edge of the current was marked
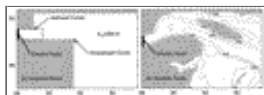
Click on thumbnail for full-sized image.

FIG. 6. Two types of model domains used in the numerical experiments. (a) the idealized basin of a flat bottom of 200 m and a piecewise-straight coastline, and (b) the realistic basin with variable bottom and irregular coastline representing the model resolved NWG bathymetry over the area marked by the dashed lines in Fig. 1 ⊙▬
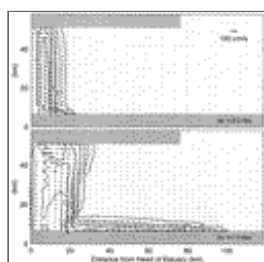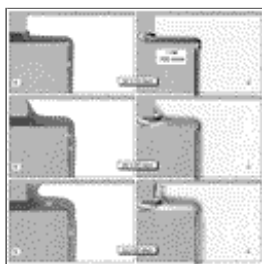

Click on thumbnail for full-sized image.

FIG. 7. Near-surface salinity and current fields over the estuary region marked by the dashed line in Fig. 6a ⬤▬ after (a) 0.2 day and (b) 1 day of simulation. The model was driven by the river discharge at the estuary head
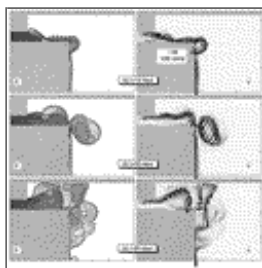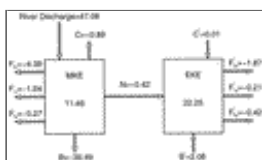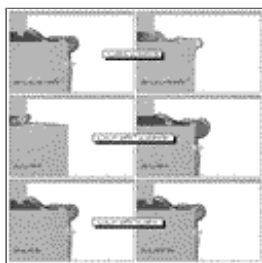

Click on thumbnail for full-sized image.

FIG. 8. Near surface salinity and flow fields in the idealized basin produced by the fully nonlinear CANDIE model at (a) day 10, (b) day 30, and (c) day 50. The model was driven by river discharge at the estuary head. The salinity contour interval is 2 ppt. The dashed salinity contour line represents the boundary between the estuarine and shelf waters. Velocity vectors are shown at every fourth grid point

Click on thumbnail for full-sized image.

FIG. 9. Near surface salinity and flow fields in the idealized basin produced by the linearized CANDIE model (i.e., the one without advection terms in the momentum equations). Otherwise as in Fig. 8 ⬤▬
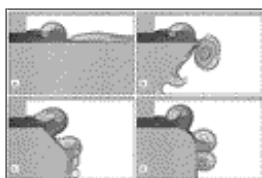

Click on thumbnail for full-sized image.

FIG. 10. Total domain kinetic energy balance for the time-mean and eddy flow in the idealized basin. All values are the volume average. Units are in $cm^2 s^{-2}$ for the energy levels and in $10^{-5} cm^2 s^{-3}$ for energy transfers
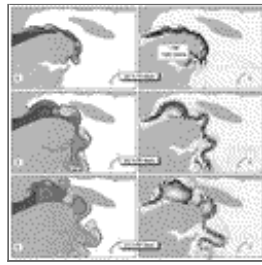

Click on thumbnail for full-sized image.

FIG. 11. Near-surface salinity at day 10 in the idealized basin forced by the river discharge at the estuary head. The model parameters are the same as in Fig. 8 ⬤▬, except the vertical mixing coefficients were changed to (a) $0.1 cm^2 s^{-1}$ and (b) $10 cm^2 s^{-1}$; the thickness of the upper waters at the estuary head was changed to (c) 10 m and (d) 40 m; and the transport of the barotropic inflow in the upper waters at the head was changed to (e) 0 Sv and (f) 0.07 Sv, respectively
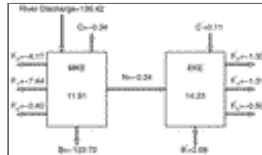

Click on thumbnail for full-sized image.

FIG. 12. Near-surface salinity at day 30 driven by the river discharge at the estuary head in the idealized basin with (a) an obtuse downstream corner, (b) a sharp downstream corner, (c) two obtuse downstream corners, and (d) a model-resolved round downstream corner. Otherwise, same as Fig. 8
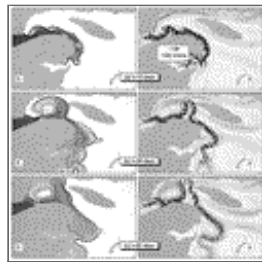

Click on thumbnail for full-sized image.

FIG. 13. Near-surface salinity and flow fields in the realistic basin driven by the river discharge at the estuary head at (a) day 10, (b) day 30, and (c) day 50. Otherwise, same as Fig. 8

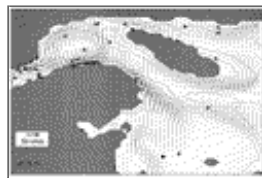Click on thumbnail for full-sized image.

FIG. 14. Total domain kinetic energy balance for the time-mean and eddy flow in the realistic basin. All values are the volume average. Units are in $cm^2 s^{-2}$ for the energy levels and in $10^{-5} cm^2 s^{-3}$ for energy transfers

Click on thumbnail for full-sized image.

FIG. 15. Near-surface salinity and flow fields in the realistic basin forced by the river discharge at the estuary head and a barotropic westward inflow at the northeast corner of the eastern open boundary at (a) day 10, (b) day 30, and (c) day 50. Otherwise, same as Fig. 13

Click on thumbnail for full-sized image.

FIG. 16. Time-mean predicted currents (solid arrows) at 15-m depth averaged from the model results between day 5 and day 80. Velocity vectors are shown at every third grid point. Open arrows are the current-meter observations made in summer with record lengths longer than 15 days in the upper ocean (10–40 m)

Corresponding author address: Dr. Jinyu Sheng, Dalhousie University, Department of Oceanography, Halifax, NS B3H 4J1, Canada. E-mail: jinyu.sheng@dal.ca